photonics

MDPI

Communication

Response Time of III-V Multistage Detectors Based on the "Ga-Free" InAs/InAsSb Type-II Superlattice

Karol Dąbrowski [1,2], Waldemar Gawron [1,2,*] and Piotr Martyniuk [1]

1 Institute of Applied Physics, Military University of Technology, 2 Kaliskiego St., 00-908 Warsaw, Poland; karol.dabrowski@wat.edu.pl or kdabrowski@vigo.com.pl (K.D.); piotr.martyniuk@wat.edu.pl (P.M.)
2 VIGO Photonics S.A., 129/133 Poznańska St., 05-850 Ożarów Mazowiecki, Poland
* Correspondence: wgawron@vigo.com.pl or waldemar.gawron@wat.edu.pl

Abstract: This paper presents a response time/time constant of III-V material-based interband long wavelength multistage infrared detector optimized for a wavelength of 10.6 µm at 200 K. The device is based on the InAs/InAsSb type-II superlattice with highly doped p^+/n^+ tunneling junctions among the stages. The detector exhibits a response time of 9.87 ns under zero voltage condition, while for 0.15 V reverse bias, that time decreases to approximately 350 ps. The presented device shows a significant increase in response time, especially for low bias, and for a voltage of −0.2 V, the decrease in the detector's response time by an order of magnitude was estimated. Higher voltage slightly affects the time constant, and between −0.3 V and −1 V, it varies between 300 and 400 ps. The significant change in the detector's response time between −0.1 V and −0.2 V probably results from electric field drop over entire absorber region. The optimal operating condition can be reached for −0.15 V, where the time constant reaches approximately 350 ns with peak detectivity at a level of ~3×10^9 Jones.

Keywords: ICIP; interband cascade detector; InAs/InAsSb superlattice; response time; time constant

check for updates

Citation: Dąbrowski, K.; Gawron, W.; Martyniuk, P. Response Time of III-V Multistage Detectors Based on the "Ga-Free" InAs/InAsSb Type-II Superlattice. *Photonics* **2024**, *11*, 224. https://doi.org/10.3390/photonics11030224

Received: 1 February 2024
Revised: 23 February 2024
Accepted: 27 February 2024
Published: 29 February 2024

1. Introduction

Infrared photon detectors, compared to other types of sensors operating in this wavelength range, are characterized by very high response speed, but many applications put extreme requirements in terms of response time on these devices. Among such applications, we can distinguish the use of detectors for the characterization of laser sources and dual comb spectroscopy for the analysis of gas composition, where response time in the ps range is needed. The response time of a photon detector is largely limited by the minority carriers' diffusion time within the absorber area, where "flat" energy bands are used to minimize noise. Applying reverse bias causes the absorber bands to bend, which leads to the faster removal of carriers from that region under the electric field. In most cases, the photodiodes operate in either zero voltage or at low bias to minimize the impact of shot noise and, consequently, maximize the devices' detectivity (D^*). This is a frequently used practice, especially in the case of long-wavelength (LWIR) detectors operating at high temperatures, where the noise resulting from thermal generation–recombination (g-r) processes is relatively high. Additionally, for LWIR devices, detectivity is further limited by the short carrier diffusion length (L) and low absorption coefficient (α), both reducing the device's quantum efficiency (QE). The issue of low QE in LWIR detectors, resulting from the short minority carrier diffusion length, low absorption coefficient ($\alpha L < 1$), and further to increase the response speed of such devices could be resolved by interband cascade infrared photodetector (ICIP) design, where thin absorbers are connected in series by tunneling regions.

Looking back over the history of cascade devices, Elliott and White were the first to present the concept of a multistage photodetector based on interband transitions in MCT by series discrete absorbers [1]. Next, it was Piotrowski who demonstrated the LWIR MCT devices built by the detector's cell horizontally connected by highly doped p^+/n^+ regions and proposed the concept of vertically stacked thin photovoltaic MCT detectors, where active layers were also connected through p^+/n^+ tunnel junctions [2,3]. The proposed solution allows for the selection of the single absorber width to be lower than the diffusion length, while the total thickness of all the absorbers should be assumed to at least be equal to the absorption depth ($1/\alpha$). Due to the high Hg diffusion, this concept was found to be difficult to implement in the case of MCT detectors. However, it turned out to be feasible in the case of detectors based on III-V semiconductors due to low interdiffusion coefficients.

There are many papers confirming the possibility of using ICIPs structures based on the III-V materials family, where Yang et al. developed a pioneering theory and presented ICIPs operating within SWIR, MWIR, and LWIR ranges based on both T2SLs InAs/GaSb and InAs/InAsSb [4–17]. As mentioned earlier, the use of a cascade structure makes it possible to improve the detector's detectivity by the increase in QE (and when biased by shot noise suppression by the number of stages, where the optimal number of stages depends on the absorption coefficient and thickness of the single absorber $N_s = 1/2\alpha d$) and to decrease the response time of such devices by a significant reduction in the single absorber thickness (reduced carrier diffusion time) [18–20].

This article presents the response time of the ICIP system supported by a GaAs immersion lens for selected voltages, operating at a temperature that can be achieved using a thermoelectric cooler, thanks to which the detector is much smaller than the one cooled with liquid nitrogen. In addition, the devices' electrical and optical performance is presented. Finally, the time constant (response time) for T2SLs InAs/InAsSb, InAs/GaSb, and MCT detectors was compared. The analyzed devices were based on "Ga-free" InAs/InAsSb T2SLs with highly doped p^+/n^+ tunneling junctions connecting adjacent stages.

2. Materials and Methods

The devices (based on T2SLs "Ga-free" heterostructure) analyzed in this paper were grown by the RIBER Compact 21-DZ solid source MBE system on a 2″ semi-insulating 1.1 mm thick GaAs (001) substrate with Si donor and Be acceptor dopants. It was designed/optimized to reach the highest possible detectivity for a wavelength of 10.6 µm at a temperature of 200 K. Figure 1 shows the architecture used for the analyzed device. It was built out of three 1 µm thick absorbers.

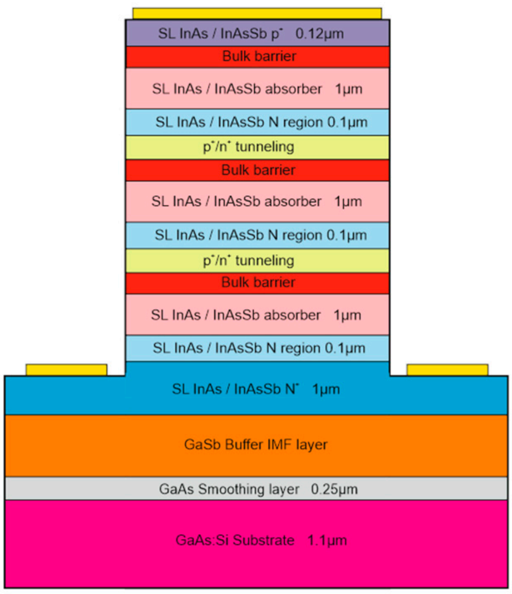

Figure 1. The LWIR InAs/InAsSb T2SL multi-junction three stages; cascade detector with p^+/n^+ connecting regions optimized for a wavelength of 10.6 µm at 200 K.

As seen in the figure above, a 250 nm GaAs smoothing layer was deposited on a GaAs substrate. Then, a GaSb buffer layer >1 µm thick was deposited to accommodate the strains between substrate and T2SLs. All subsequent layers, except the <0.2 µm thick barrier, were made of T2SLs. A more detailed analysis of the T2SLs InAs/InAsSb layers is as follows:

- 1 µm thick InAs/InAsSb N^+ contact layer;
- 0.1 µm thick InAs/InAsSb N layer serving as the electron contact and hole barrier;
- 1 µm thick InAs/InAsSb T2SLs absorber (10.5 nm period T2SLs: InAs 7.99 nm/InAsSb 2.51 nm, $x_{Sb} = 0.39$);
- Heavily doped p^+/n^+ tunnel junctions with the same design as the absorbers;
- 0.12 µm thick InAs/InAsSb p^+ contact layer.

The wet chemical etching and standard photolithography techniques were implemented to delineate a mesa structure with an area of 0.01 mm^2. The Ti/Pt adhesion layer and Au contact layers were deposited as the ohmic contact by a sputtering method. The device was not passivated, which is why for higher voltages, the leakage current was observed.

The epitaxial heterostructure was tested by the HRXRD measurement taken in the 2Θ-ω direction. The results of this measurement are shown in Figure 2. The peak for the angle of 66.05 represents GaAs substrate, and the peak for 60.9° represents the bulk barrier that was not taken into account in the simulation. Satellites visible for the angles between 55 and 60.5° and 55° and 64.7° correspond to the absorber T2SLs and N^+ T2SLs, respectively. The FWHM of the 0th order satellite was estimated at the level of ~200 arcsec.

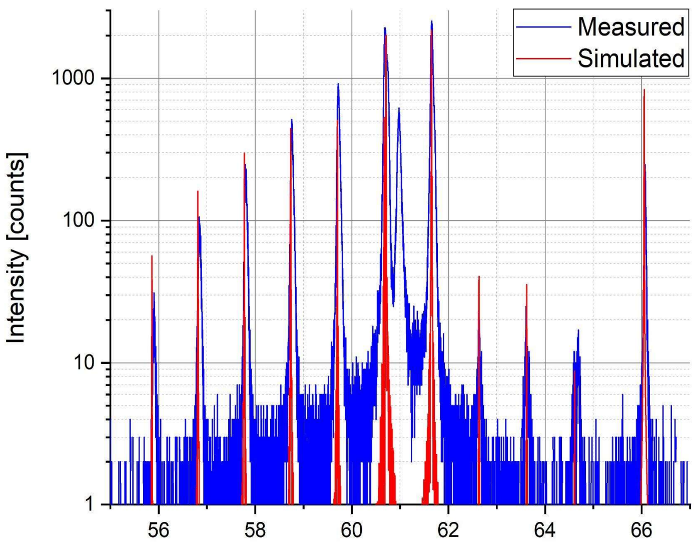

Figure 2. The HRXRD spectrum (blue) with T2SLs simulation (red) for three-stage 1 µm thick single absorber device.

The presented ICIP structure was based on the three 1 µm thick absorbers. To maximize the device's performance, the GaAs immersion lens was mechanically polished, followed by a flip-chip of the detector's structure onto the sapphire pad. To enable stable operation at a temperature of 200 K, the device was mounted on a four-stage thermoelectric (TE) cooler and then closed in an inert gas atmosphere (Kr/Xe) using TO8 package. An antireflective (AR) ZnSe window was selected.

The detectors' response time measurement was performed by the set-up specially prepared for this purpose, which is shown in Figure 3.

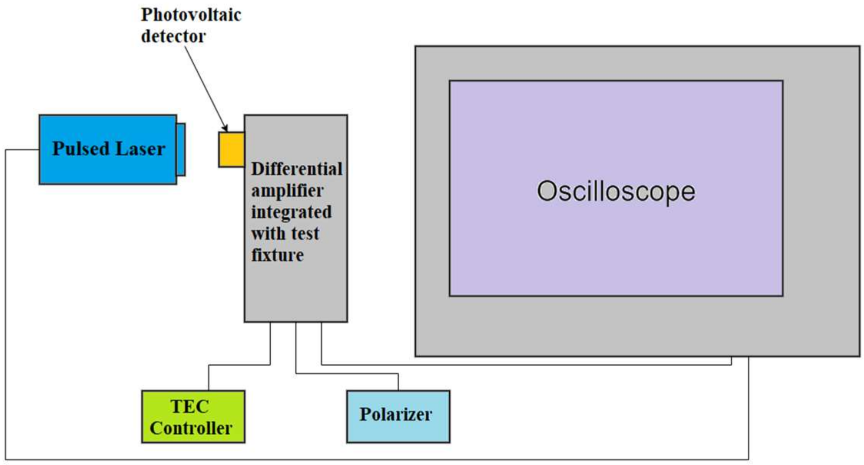

Figure 3. Block diagram of the response time measurement set-up.

Voltage versus time was measured by a pulsed laser with steep slopes and an operating wavelength of 4.986 μm. The slope falling time ranged between 120 and 180 ps (between 90% and 10% of the peak value). To shorten the path between the structure and the amplifier, the higher-speed differential amplifier integrated with the test fixture was used. Additionally, a detector power supply and cooler controllers were also applied to stabilize the polarization and temperature. Data were registered by an oscilloscope programmed to read the time between the assumed values of 90% and 10% of the maximum signal. The detector was mounted at a distance of 10 cm from the radiation source.

3. Results

3.1. Detector Parameters

The current–voltage characteristics (Figure 4a) and current sensitivity were performed for selected voltages (Figure 4c) within the range between 0 and −1 V. Due to the influence of the voltage on the response time (even for low values), the measurement points were concentrated within the region up to −0.2 V. In Figure 4a, one can observe the lack of saturation of the I-V curve and the significant increase in the current for V > −0.3 V. The current–voltage linear dependence for V > −0.4 V confirms the surface contribution. Based on the current–voltage characteristic, a dynamic resistance was recalculated, and this is shown in Figure 4b. Spectral response was measured by an FTIR spectrometer and a calibrated 800 K blackbody source.

Based on Figure 4c, it can be concluded that the maximum current responsivity, regardless of voltage, ranges between 0.6 and 0.7 A/W, and for a wavelength of 10.6 μm, this value is approximately 0.2 A/W. Based on the two above measurements, the device detectivity for selected voltages was determined according to the following expression:

$$D^* = R_i\, A^{1/2}/(4k_B T/R_d + 2eI)^{1/2}, \quad (1)$$

where R_i is the current sensitivity of the detector, A is the active surface area, k_B is the Boltzmann constant, T is the temperature, e is the electric charge, R_d is the dynamic resistance, and I stands for the current of the given voltage.

Detectivity for unbiased condition reaches ~1.2×10^{10} Jones and decreases versus voltage to ~2.4×10^9 Jones at 1 V reverse bias. Interestingly, as Figure 5 shows, the D^* tends to saturate versus voltage. The responsivity and detectivity for selected voltages are summarized in Table 1.

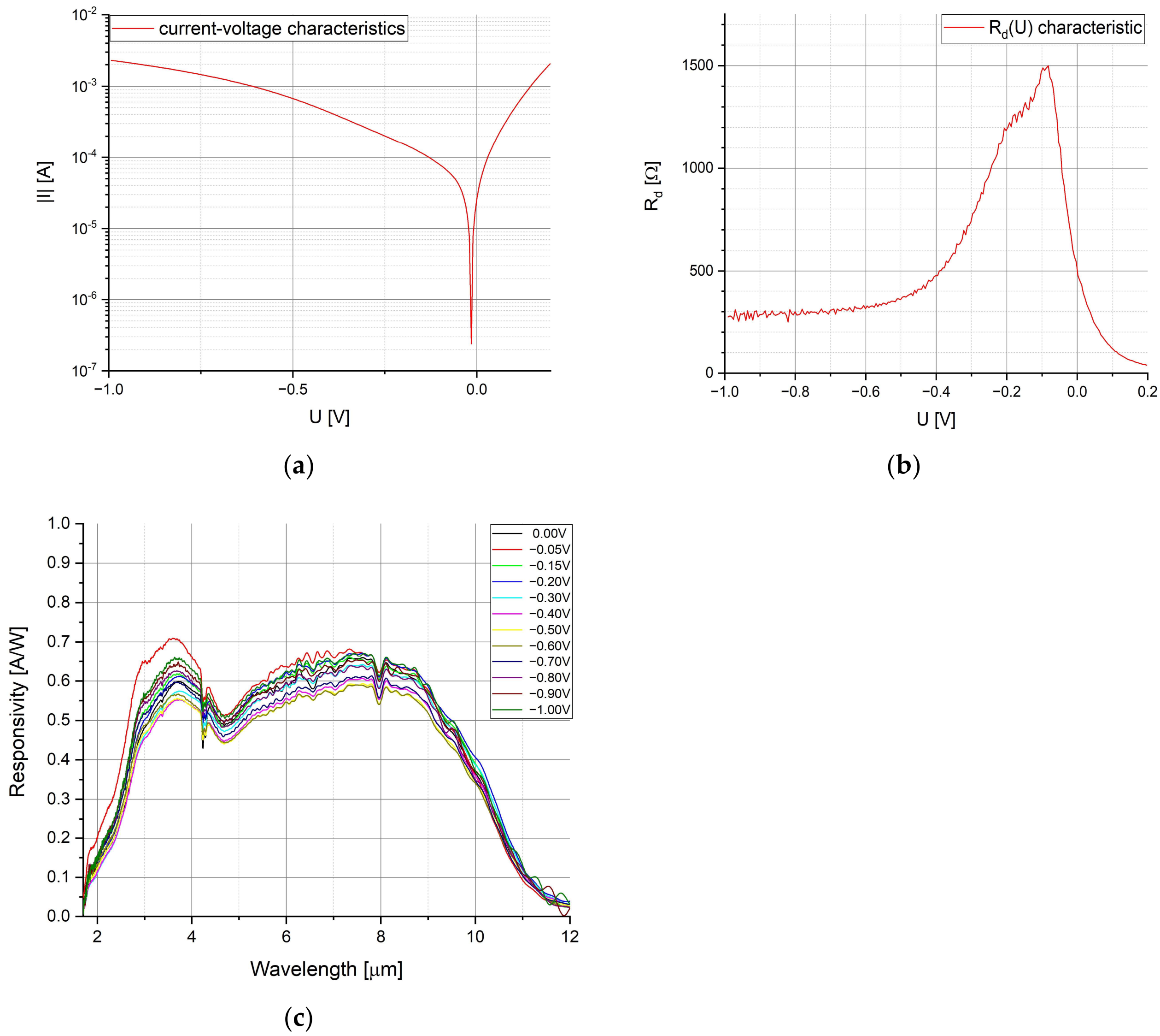

Figure 4. Current–voltage characteristics of the analyzed device (**a**), dynamic resistance as a function of voltage (**b**), and spectral characteristics of the detector for selected voltages (**c**); T = 200 K.

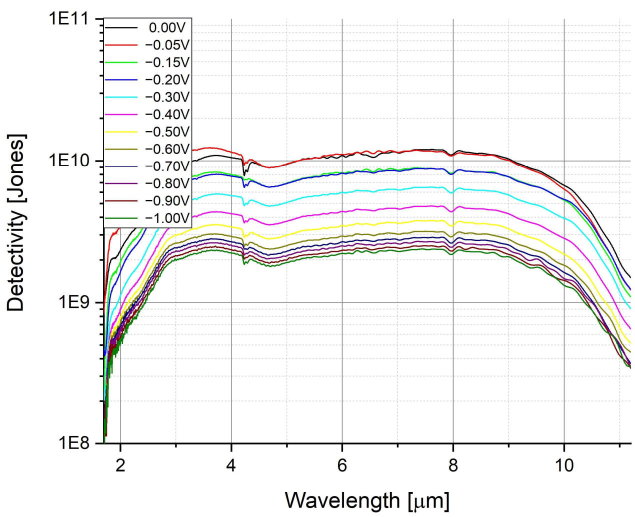

Figure 5. Detectivity for selected voltages.

Table 1. Summary of the current responsivity and detectivity for ICIP detector at 200 K for selected voltages.

Voltage [V]	Current Responsivity Peak [A/W]	Current Responsivity 10.6 µm [A/W]	Detectivity Peak [Jones]	Detectivity 10.6 µm [Jones]
0.00	0.66	0.20	1.2×10^{10}	3.7×10^{9}
−0.05	0.68	0.18	1.2×10^{10}	3.2×10^{9}
−0.10	0.66	0.21	1.4×10^{10}	3.9×10^{9}
−0.15	0.66	0.21	8.8×10^{9}	3.2×10^{9}
−0.20	0.67	0.23	8.8×10^{9}	2.8×10^{9}
−0.30	0.64	0.22	6.5×10^{9}	3.1×10^{9}
−0.40	0.61	0.20	4.8×10^{9}	2.3×10^{9}
−0.50	0.60	0.19	3.8×10^{9}	1.6×10^{9}
−0.60	0.59	0.19	3.2×10^{9}	1.2×10^{9}
−0.70	0.61	0.19	2.9×10^{9}	1.0×10^{9}
−0.80	0.64	0.21	2.7×10^{9}	9.1×10^{8}
−0.90	0.65	0.20	2.5×10^{9}	8.9×10^{8}
−1.00	0.67	0.22	2.4×10^{9}	7.8×10^{8}

3.2. ICIP Response Time

The ICIP response time was reported for MWIR devices showing great potential for this solution, enabling the combination of fast detector response time with high detectivity [18–20]. It was reported that response time depends on the proper band alignment among the detector stages [20].

Time response measurements were performed for voltages up to −1 V at a temperature of 200 K. In order to better illustrate changes in the response time, the maximum signal versus time was normalized to unity. Additionally, the detector response time was converted into time constants and compared according to the formula below:

$$t_f = 2.2\ \tau, \tag{2}$$

where t_f is the signal decay time between 90% and 10% of the signal maximum, and τ is the time constant.

Figure 6a shows the detector's time response for selected voltages, while Figure 6b depicts the time constant versus bias. In addition, the response time and time constant are listed in Table 2.

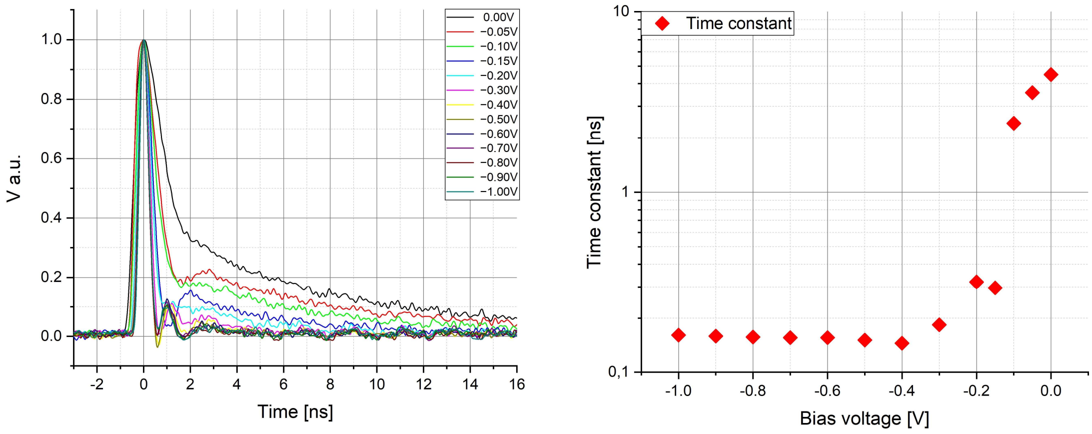

(**a**) (**b**)

Figure 6. Time response dependence on time (**a**) and time constant versus voltage (**b**).

Table 2. Summary of response time and time constant for selected voltages.

Voltage [V]	Response Time [ns]	Time Constant [ns]
0.00	9.870	4.490
−0.05	7.820	3.560
−0.10	5.300	2.410
−0.15	0.650	0.296
−0.20	0.703	0.320
−0.30	0.404	0.184
−0.40	0.319	0.145
−0.50	0.330	0.151
−0.60	0.344	0.156
−0.70	0.343	0.156
−0.80	0.345	0.157
−0.90	0.350	0.159
−1.00	0.355	0.161

As shown in Figure 6a,b and Table 2, the analyzed ICIP at 200 K and unbiased condition reaches 9.87 ns response time. The device shows a significant increase in the response time, especially for low bias, and for a voltage of −0.2 V, we can already see a decrease in the detector response time by an order of magnitude. Higher voltage slightly affects the time constant, and between −0.3 V and −1 V, it varies between 300 and 400 ps. The noticeable change in the detector's response time in the range from −0.1 V to −0.2 V is due to the electric field penetrating deeper and deeper into the absorbers, which results in an increase in the collection rate of optically generated current carriers.

3.3. Response Time Comparison for Selected MCT and T2SLs InAs/InAsSb Type Detectors

Table 3 shows a summary of the response time and time constants under zero voltage condition for PVM (photovoltaic multi-junction detector), PVI (photovoltaic detector), ICIP, and PC (photoconductive detector) (1×1 mm^2) with GaAs immersion optimized for a wavelength of 10.6 µm at 200 K. The response time for PVM, PVI, and PCI detectors was measured for the commercial devices fabricated at VIGO PHOTONICS and is consistent with the VIGO catalogue [21].

Table 3. Response time comparison for selected MCT and T2SLs InAs/InAsSb type detectors optimized for wavelength of 10.6 µm at 200 K (PVMI 50% cut-off 11.5 µm).

Absorber Material	Detector Type	Response Time [ns]	Time Constant [ns]
MCT	PVMI	4.1	1.9
	PCI	9.4	4.3
	PVI	9.0	4.1
T2SLs InAs/InAsSb	PCI	19.0	8.6
	ICIP	9.9	4.5

Based on the results presented in the table above, it can be seen that under zero voltage conditions, the lowest response time, 4.1 ns, among the analyzed devices was reached by PVMI MCT. That was related to the 50% cut-off wavelength of 11.5 µm. When comparing D^* for 10.6 µm, both PVMI and ICIP reach the same level, while for 7 µm, PVMI D^* is 50% lower than ICIP. The time response is approximately two times higher in the case of MCT PVI and PCI detectors, as well as the T2SLs ICIP detectors reaching 9–10 ns. The response time of 19 ns was reached by T2SLs PCI detectors.

4. Conclusions

The device in this study was fabricated based on the LWIR InAs/InAsSb T2SLs with highly doped p^+/n^+ tunneling junctions among stages, optimized for a wavelength of 10.6 µm at a temperature of 200 K, where a time response of 9.87 ns was reached with a voltage of >-0.2 V 300–400 ps. The peak current sensitivity stays at the level of 0.6–0.7 A/W, but the peak detectivities show a strong dependence on the voltage, and for unbiased conditions, it reaches 1.2×10^{10} Jones, while it decreases compared to voltage at 2.4×10^{9} Jones for -1 V. The results presented in this paper indicate that the optimal operating condition can be reached for -0.15 V, where the time constant reaches approximately 0.35 ns with a corresponding peak detectivity of ~3×10^{9} Jones. The presented performance shows potential for LWIR devices exhibiting frequency up to 1 GHz using standard detector assembly technologies commonly used on the market.

Author Contributions: Conceptualization, W.G. and P.M.; data curation, K.D.; formal analysis, K.D., W.G. and P.M.; funding acquisition, P.M. and W.G.; investigation, K.D.; methodology, P.M.; project administration, P.M.; software, K.D.; validation, P.M.; visualization, K.D.; writing—original draft, K.D.; writing—review and editing, P.M. and W.G. All authors have read and agreed to the published version of the manuscript.

Funding: The authors would like to acknowledge the support by National Science Centre grant: OPUS UMO-2021/43/B/ST7/00768 and The National Centre for Research and Development grant: POLTAJ10/2022/37/LWIRPSBDA/2023.

Data Availability Statement: Data are contained within the article.

Conflicts of Interest: The authors declare no conflicts of interest.

References

1. Yang, R. Signal, noises, and detectivities in multi-stage infrared photodetectors. *Proc. SPIE* **2023**, *12430*, 69–78. [CrossRef]
2. Gawron, W.; Piotrowski, J. Practical near-room temperature, long-wavelength IR photovoltaic detectors. *Opto-Electron. Rev.* **1994**, *2*, 91–94.
3. Piotrowski, J.; Gawron, W. Extension of longwavelength IR photovoltaic detector operation to near room-temperatures. *Infrared Phys. Technol.* **1995**, *36*, 1045–1051. [CrossRef]
4. Li, J.V.; Yang, R.Q.; Hill, C.J.; Chuang, S.L. Interband cascade detectors with room temperature photovoltaic operation. *Appl. Phys. Lett.* **2005**, *86*, 101102. [CrossRef]
5. Yang, R.Q.; Tian, Z.; Cai, Z.; Klem, J.F.; Johnson, M.B.; Liu, H.C. Interband-cascade infrared photodetectors with superlattice absorbers. *J. Appl. Phys.* **2010**, *107*, 054514. [CrossRef]
6. Yang, R.Q.; Tian, Z.; Klem, J.F.; Mishima, T.D.; Santos, M.B.; Johnson, M.B. Interband cascade photovoltaic devices. *Appl. Phys. Lett.* **2010**, *96*, 063504. [CrossRef]
7. Tian, Z.; Hinkey, R.T.; Yang, R.Q.; Lubyshev, D.; Qiu, Y.; Fastenau, J.M.; Liu, W.K.; Johnson, M.B. Interband cascade infrared photodetectors with enhanced electron barriers and p-type superlattice absorbers. *J. Appl. Phys.* **2012**, *111*, 024510. [CrossRef]
8. Yang, R.Q.; Li, L.; Zhao, L.; Jiang, Y.; Tian, Z.; Ye, H.; Hinkey, R.T.; Niu, C.; Mishima, T.D.; Santos, M.B.; et al. Recent progress in development of InAs-based interband cascade lasers. *Proc. SPIE* **2013**, *8640*, 84–93. [CrossRef]
9. Hackiewicz, K.; Rutkowski, J.; Martyniuk, P. Optimal absorber thickness in interband cascade photodetectors. *Infrared Phys. Technol.* **2018**, *95*, 136–140. [CrossRef]
10. Gautam, N.; Myers, S.; Barve, A.V.; Klein, B.; Smith, E.P.; Rhiger, D.R.; Dawson, L.R.; Krishna, S. High operating temperature interband cascade midwave infrared detector based on type-II InAs/GaSb strained layer superlattice. *Appl. Phys. Lett.* **2012**, *101*, 021106. [CrossRef]
11. Bader, A.; Rothmayr, F.; Khan, N.; Jabeen, F.; Koeth, J.; Höfling, S.; Hartmann, F. Interband cascade infrared photodetectors based on Ga-free InAs/InAsSb superlattice absorbers. *Appl. Phys. Lett.* **2022**, *121*, 041104. [CrossRef]
12. Kubiszyn, Ł.; Michalczewski, K.; Gawron, W.; Dąbrowski, K.; Martyniuk, P. Current state of the art and the future prospect of the interband cascade photodetectors. *Proc. SPIE* **2023**, *12534*, 125341G. [CrossRef]
13. Gawron, W.; Kubiszyn, Ł.; Michalczewski, K.; Jureńczyk, J.; Piotrowski, J.; Martyniuk, P. Demonstration of T2SLs InAs/InAsSb Based Interband Cascade Detector Supported by Immersion Lens for LWIR. *J. Electron. Mater.* **2023**, *52*, 7068–7073. [CrossRef]
14. Gawron, W.; Kubiszyn, Ł.; Michalczewski, K.; Manyk, T.; Piotrowski, J.; Martyniuk, P. The performance of the ICIP Ga-free superlattice longwave infrared photodetector for high operating temperature. *Infrared Phys. Technol.* **2023**, *128*, 104499. [CrossRef]
15. Hinkey, R.T.; Yang, R.Q. Theory of multiple-stage interband photovoltaic devices and ultimate performance limit comparison of multiple-stage and single-stage interband infrared detectors. *J. Appl. Phys.* **2013**, *114*, 104506. [CrossRef]
16. Martyniuk, P.; Rogalski, A.; Krishna, S. Interband Quantum Cascade Infrared Photodetectors: Current Status and Future Trends. *Phys. Rev. Appl.* **2022**, *17*, 027001. [CrossRef]
17. Lei, L.; Li, L.; Ye, H.; Lotfi, H.; Yang, R.; Johnson, M.; Massengale, J.; Mishima, D.; Santos, M. Long wavelength interband cascade infrared photodetectors operating at high temperatures. *J. Appl. Phys.* **2016**, *120*, 193102. [CrossRef]
18. Lotfi, H.; Li, L.; Lei, L.; Ye, H.; Rassel, S.M.S.; Jiang, Y.; Yang, R.Q.; Mishima, T.D.; Santos, M.B.; Gupta, J.A.; et al. High-frequency operation of a mid-infrared interband cascade system at room temperature. *Appl. Phys. Lett* **2016**, *108*, 201101. [CrossRef]

19. Xie, Z.; Huang, J.; Chai, X.; Deng, Z.; Chen, Y.; Lu, Q.; Xu, Z.; Chen, J.; Zhou, Y.; Chen, B. High-speed mid-wave infrared interband cascade photodetector at room temperature. *Opt. Express* **2020**, *28*, 36915–36923. [CrossRef] [PubMed]
20. Pusz, W.; Kowalewski, A.; Martyniuk, P.; Gawron, W.; Pils, E.; Krishna, S.; Rogalski, A. Mid-wavelength infrared type-II InAs/GaSb superlattice interband cascade photodetectors. *Opt. Eng.* **2014**, *53*, 043107. [CrossRef]
21. Available online: https://vigophotonics.com/products/infrared-detectors/ (accessed on 1 January 2024).